Letter

Global Λ-hyperon polarization in Au + Au collisions at $\sqrt{s_{NN}} = 3$ GeV

M. S. Abdallah,[5] B. E. Aboona,[55] J. Adam,[6] L. Adamczyk,[2] J. R. Adams[39] J. K. Adkins,[30] G. Agakishiev,[28] I. Aggarwal,[41] M. M. Aggarwal,[41] Z. Ahammed,[60] I. Alekseev,[3,35] D. M. Anderson,[55] A. Aparin,[28] E. C. Aschenauer,[6] M. U. Ashraf,[11] F. G. Atetalla,[29] A. Attri,[41] G. S. Averichev,[28] V. Bairathi,[53] W. Baker,[10] J. G. Ball Cap,[20] K. Barish,[10] A. Behera,[52] R. Bellwied,[20] P. Bhagat,[27] A. Bhasin,[27] J. Bielcik,[14] J. Bielcikova,[38] I. G. Bordyuzhin,[3] J. D. Brandenburg,[6] A. V. Brandin,[35] I. Bunzarov,[28] J. Butterworth,[45] X. Z. Cai,[50] H. Caines,[63] M. Calderón de la Barca Sánchez,[8] D. Cebra,[8] I. Chakaberia,[31,6] P. Chaloupka,[14] B. K. Chan,[9] F.-H. Chang,[37] Z. Chang,[6] N. Chankova-Bunzarova,[28] A. Chatterjee,[11] S. Chattopadhyay,[60] D. Chen,[10] J. Chen,[49] J. H. Chen,[18] X. Chen,[48] Z. Chen,[49] J. Cheng,[57] M. Chevalier,[10] S. Choudhury,[18] W. Christie,[6] X. Chu,[6] H. J. Crawford,[7] M. Csanád,[16] M. Daugherity,[1] T. G. Dedovich,[28] I. M. Deppner,[19] A. A. Derevschikov,[43] A. Dhamija,[41] L. Di Carlo,[62] L. Didenko,[6] P. Dixit,[22] X. Dong,[31] J. L. Drachenberg,[1] E. Duckworth,[29] J. C. Dunlop,[6] N. Elsey,[62] J. Engelage,[7] G. Eppley,[45] S. Esumi,[58] O. Evdokimov,[12] A. Ewigleben,[32] O. Eyser,[6] R. Fatemi,[30] F. M. Fawzi,[5] S. Fazio,[6] P. Federic,[38] J. Fedorisin,[28] C. J. Feng,[37] Y. Feng,[44] P. Filip,[28] E. Finch,[51] Y. Fisyak,[6] A. Francisco,[63] C. Fu,[11] L. Fulek,[2] C. A. Gagliardi,[55] T. Galatyuk,[15] F. Geurts,[45] N. Ghimire,[54] A. Gibson,[59] K. Gopal,[23] X. Gou,[49] D. Grosnick,[59] A. Gupta,[27] W. Guryn,[6] A. I. Hamad,[29] A. Hamed,[5] Y. Han,[45] S. Harabasz,[15] M. D. Harasty,[8] J. W. Harris,[63] H. Harrison,[30] S. He,[11] W. He,[18] X. H. He,[26] Y. He,[49] S. Heppelmann,[8] S. Heppelmann,[42] N. Herrmann,[19] E. Hoffman,[20] L. Holub,[14] Y. Hu,[18] H. Huang,[37] H. Z. Huang,[9] S. L. Huang,[52] T. Huang,[37] X. Huang,[57] Y. Huang,[57] T. J. Humanic,[39] G. Igo,[9,*] D. Isenhower,[1] W. W. Jacobs,[25] C. Jena,[23] A. Jentsch,[6] Y. Ji,[31] J. Jia,[6,52] K. Jiang,[48] X. Ju,[48] E. G. Judd,[7] S. Kabana,[53] M. L. Kabir,[10] S. Kagamaster,[32] D. Kalinkin,[25,6] K. Kang,[57] D. Kapukchyan,[10] K. Kauder,[6] H. W. Ke,[6] D. Keane,[29] A. Kechechyan,[28] M. Kelsey,[62] Y. V. Khyzhniak,[35] D. P. Kikoła,[61] C. Kim,[10] B. Kimelman,[8] D. Kincses,[16] I. Kisel,[17] A. Kiselev,[6] A. G. Knospe,[32] H. S. Ko,[31] L. Kochenda,[35] L. K. Kosarzewski,[14] L. Kramarik,[14] P. Kravtsov,[35] L. Kumar,[41] S. Kumar,[26] R. Kunnawalkam Elayavalli,[63] J. H. Kwasizur,[25] R. Lacey,[52] S. Lan,[11] J. M. Landgraf,[6] J. Lauret,[6] A. Lebedev,[6] R. Lednicky,[28,38] J. H. Lee,[6] Y. H. Leung,[31] C. Li,[49] C. Li,[48] W. Li,[45] X. Li,[48] Y. Li,[57] X. Liang,[10] Y. Liang,[29] R. Licenik,[38] T. Lin,[49] Y. Lin,[11] M. A. Lisa,[39] F. Liu,[11] H. Liu,[25] H. Liu,[11] P. Liu,[52] T. Liu,[63] X. Liu,[39] Y. Liu,[55] Z. Liu,[48] T. Ljubicic,[6] W. J. Llope,[62] R. S. Longacre,[6] E. Loyd,[10] N. S. Lukow,[54] X. F. Luo,[11] L. Ma,[18] R. Ma,[6] Y. G. Ma,[18] N. Magdy,[12] D. Mallick,[36] S. Margetis,[29] C. Markert,[56] H. S. Matis,[31] J. A. Mazer,[46] N. G. Minaev,[43] S. Mioduszewski,[55] B. Mohanty,[36] M. M. Mondal,[52] I. Mooney,[62] D. A. Morozov,[43] A. Mukherjee,[16] M. Nagy,[16] J. D. Nam,[54] Md. Nasim,[22] K. Nayak,[11] D. Neff,[9] J. M. Nelson,[7] D. B. Nemes,[63] M. Nie,[49] G. Nigmatkulov,[35] T. Niida,[58] R. Nishitani,[58] L. V. Nogach,[43] T. Nonaka,[58] A. S. Nunes,[6] G. Odyniec,[31] A. Ogawa,[6] S. Oh,[31] V. A. Okorokov,[35] B. S. Page,[6] R. Pak,[6] J. Pan,[55] A. Pandav,[36] A. K. Pandey,[58] Y. Panebratsev,[28] P. Parfenov,[35] B. Pawlik,[40] D. Pawlowska,[61] H. Pei,[11] C. Perkins,[7] L. Pinsky,[20] R. L. Pintér,[16] J. Pluta,[61] B. R. Pokhrel,[54] G. Ponimatkin,[38] J. Porter,[31] M. Posik,[54] V. Prozorova,[14] N. K. Pruthi,[41] M. Przybycien,[2] J. Putschke,[62] H. Qiu,[26] A. Quintero,[54] C. Racz,[10] S. K. Radhakrishnan,[29] N. Raha,[62] R. L. Ray,[56] R. Reed,[32] H. G. Ritter,[31] M. Robotkova,[38] O. V. Rogachevskiy,[28] J. L. Romero,[8] D. Roy,[46] L. Ruan,[6] J. Rusnak,[38] N. R. Sahoo,[49] H. Sako,[58] S. Salur,[46] J. Sandweiss,[63,*] S. Sato,[58] W. B. Schmidke,[6] N. Schmitz,[33] B. R. Schweid,[52] F. Seck,[15] J. Seger,[13] M. Sergeeva,[9] R. Seto,[10] P. Seyboth,[33] N. Shah,[24] E. Shahaliev,[28] P. V. Shanmuganathan,[6] M. Shao,[48] T. Shao,[18] A. I. Sheikh,[29] D. Shen,[50] S. S. Shi,[11] Y. Shi,[49] Q. Y. Shou,[18] E. P. Sichtermann,[31] R. Sikora,[2] M. Simko,[38] J. Singh,[41] S. Singha,[26] M. J. Skoby,[44] N. Smirnov,[63] Y. Söhngen,[19] W. Solyst,[25] P. Sorensen,[6] H. M. Spinka,[4,*] B. Srivastava,[44] T. D. S. Stanislaus,[59] M. Stefaniak,[61] D. J. Stewart,[63] M. Strikhanov,[35] B. Stringfellow,[44] A. A. P. Suaide,[47] M. Sumbera,[38] B. Summa,[42] X. M. Sun,[11] X. Sun,[12] Y. Sun,[48] Y. Sun,[21] B. Surrow,[54] D. N. Svirida,[3] Z. W. Sweger,[8] P. Szymanski,[61] A. H. Tang,[6] Z. Tang,[48] A. Taranenko,[35] T. Tarnowsky,[34] J. H. Thomas,[31] A. R. Timmins,[20] D. Tlusty,[13] T. Todoroki,[58] M. Tokarev,[28] C. A. Tomkiel,[32] S. Trentalange,[9] R. E. Tribble,[55] P. Tribedy,[6] S. K. Tripathy,[16] T. Truhlar,[14] B. A. Trzeciak,[14] O. D. Tsai,[9] Z. Tu,[6] T. Ullrich,[6] D. G. Underwood,[4,59] I. Upsal,[49,6] G. Van Buren,[6] J. Vanek,[38] A. N. Vasiliev,[43] I. Vassiliev,[17] V. Verkest,[62] F. Videbæk,[6] S. Vokal,[28] S. A. Voloshin,[62] F. Wang,[44] G. Wang,[9] J. S. Wang,[21] P. Wang,[48] Y. Wang,[11] Y. Wang,[57] Z. Wang,[49] J. C. Webb,[6] P. C. Weidenkaff,[19] L. Wen,[9] G. D. Westfall,[34] H. Wieman,[31] S. W. Wissink,[25] J. Wu,[26] Y. Wu,[10] B. Xi,[50] Z. G. Xiao,[57] G. Xie,[31] W. Xie,[44] H. Xu,[21] N. Xu,[31] Q. H. Xu,[49] Y. Xu,[49] Z. Xu,[6] Z. Xu,[9] C. Yang,[49] Q. Yang,[49] S. Yang,[45] Y. Yang,[37] Z. Ye,[45] Z. Ye,[12] L. Yi,[49] K. Yip,[6] Y. Yu,[49] H. Zbroszczyk,[61] W. Zha,[48] C. Zhang,[52] D. Zhang,[11] J. Zhang,[49] S. Zhang,[12] S. Zhang,[18] X. P. Zhang,[57] Y. Zhang,[26] Y. Zhang,[48] Y. Zhang,[11] Z. J. Zhang,[37] Z. Zhang,[6] Z. Zhang,[12] J. Zhao,[44] C. Zhou,[18] X. Zhu,[57] M. Zurek,[4] and M. Zyzak[17]

(STAR Collaboration)

[1] *Abilene Christian University, Abilene, Texas 79699*
[2] *AGH University of Science and Technology, FPACS, Cracow 30-059, Poland*
[3] *Alikhanov Institute for Theoretical and Experimental Physics NRC "Kurchatov Institute", Moscow 117218, Russia*
[4] *Argonne National Laboratory, Argonne, Illinois 60439*

---

*Deceased.

[5]*American University of Cairo, New Cairo 11835, New Cairo, Egypt*
[6]*Brookhaven National Laboratory, Upton, New York 11973*
[7]*University of California, Berkeley, California 94720*
[8]*University of California, Davis, California 95616*
[9]*University of California, Los Angeles, California 90095*
[10]*University of California, Riverside, California 92521*
[11]*Central China Normal University, Wuhan, Hubei 430079*
[12]*University of Illinois at Chicago, Chicago, Illinois 60607*
[13]*Creighton University, Omaha, Nebraska 68178*
[14]*Czech Technical University in Prague, FNSPE, Prague 115 19, Czech Republic*
[15]*Technische Universität Darmstadt, Darmstadt 64289, Germany*
[16]*ELTE Eötvös Loránd University, Budapest, Hungary H-1117*
[17]*Frankfurt Institute for Advanced Studies FIAS, Frankfurt 60438, Germany*
[18]*Fudan University, Shanghai, 200433*
[19]*University of Heidelberg, Heidelberg 69120, Germany*
[20]*University of Houston, Houston, Texas 77204*
[21]*Huzhou University, Huzhou, Zhejiang 313000*
[22]*Indian Institute of Science Education and Research (IISER), Berhampur 760010, India*
[23]*Indian Institute of Science Education and Research (IISER) Tirupati, Tirupati 517507, India*
[24]*Indian Institute Technology, Patna, Bihar 801106, India*
[25]*Indiana University, Bloomington, Indiana 47408*
[26]*Institute of Modern Physics, Chinese Academy of Sciences, Lanzhou, Gansu 730000*
[27]*University of Jammu, Jammu 180001, India*
[28]*Joint Institute for Nuclear Research, Dubna 141 980, Russia*
[29]*Kent State University, Kent, Ohio 44242*
[30]*University of Kentucky, Lexington, Kentucky 40506-0055*
[31]*Lawrence Berkeley National Laboratory, Berkeley, California 94720*
[32]*Lehigh University, Bethlehem, Pennsylvania 18015*
[33]*Max-Planck-Institut für Physik, Munich 80805, Germany*
[34]*Michigan State University, East Lansing, Michigan 48824*
[35]*National Research Nuclear University MEPhI, Moscow 115409, Russia*
[36]*National Institute of Science Education and Research, HBNI, Jatni 752050, India*
[37]*National Cheng Kung University, Tainan 70101*
[38]*Nuclear Physics Institute of the CAS, Rez 250 68, Czech Republic*
[39]*Ohio State University, Columbus, Ohio 43210*
[40]*Institute of Nuclear Physics PAN, Cracow 31-342, Poland*
[41]*Panjab University, Chandigarh 160014, India*
[42]*Pennsylvania State University, University Park, Pennsylvania 16802*
[43]*NRC "Kurchatov Institute", Institute of High Energy Physics, Protvino 142281, Russia*
[44]*Purdue University, West Lafayette, Indiana 47907*
[45]*Rice University, Houston, Texas 77251*
[46]*Rutgers University, Piscataway, New Jersey 08854*
[47]*Universidade de São Paulo, São Paulo, Brazil 05314-970*
[48]*University of Science and Technology of China, Hefei, Anhui 230026*
[49]*Shandong University, Qingdao, Shandong 266237*
[50]*Shanghai Institute of Applied Physics, Chinese Academy of Sciences, Shanghai 201800*
[51]*Southern Connecticut State University, New Haven, Connecticut 06515*
[52]*State University of New York, Stony Brook, New York 11794*
[53]*Instituto de Alta Investigación, Universidad de Tarapacá, Arica 1000000, Chile*
[54]*Temple University, Philadelphia, Pennsylvania 19122*
[55]*Texas A&M University, College Station, Texas 77843*
[56]*University of Texas, Austin, Texas 78712*
[57]*Tsinghua University, Beijing 100084*
[58]*University of Tsukuba, Tsukuba, Ibaraki 305-8571, Japan*
[59]*Valparaiso University, Valparaiso, Indiana 46383*
[60]*Variable Energy Cyclotron Centre, Kolkata 700064, India*
[61]*Warsaw University of Technology, Warsaw 00-661, Poland*

^{62}*Wayne State University, Detroit, Michigan 48201*
^{63}*Yale University, New Haven, Connecticut 06520*

Global hyperon polarization, $\overline{P}_H$, in Au + Au collisions over a large range of collision energy, $\sqrt{s_{NN}}$, was recently measured and successfully reproduced by hydrodynamic and transport models with intense fluid vorticity of the quark-gluon plasma. While naïve extrapolation of data trends suggests a large $\overline{P}_H$ as the collision energy is reduced, the behavior of $\overline{P}_H$ at small $\sqrt{s_{NN}} < 7.7$ GeV is unknown. Operating the STAR experiment in fixed-target mode, we measured the polarization of Λ hyperons along the direction of global angular momentum in Au + Au collisions at $\sqrt{s_{NN}} = 3$ GeV. The observation of substantial polarization of $4.91 \pm 0.81(\text{stat.}) \pm 0.15(\text{syst.})\%$ in these collisions may require a reexamination of the viscosity of any fluid created in the collision, of the thermalization timescale of rotational modes, and of hadronic mechanisms to produce global polarization.

Collisions between heavy nuclei at the highest energies at the Relativistic Heavy Ion Collider (RHIC) and the Large Hadron Collider (LHC) produce the quark-gluon plasma (QGP), a strongly interacting system characterized by colored degrees of freedom [1]. Viscous relativistic hydrodynamics is one of the most powerful tools to understand this system theoretically [2]; it is the dynamical heart of the "standard model of the Little Bang" [3]. Systematic comparisons of data and the hydrodynamic response to anisotropies in the initial state have yielded considerable insight on transport coefficients and the equation of state of the QGP [4]. Recently, considerable experimental and theoretical efforts have focused on the polarization of particles emitted from the fluid [5]—mostly Λ hyperons [6–11] and, very recently, multistrange hyperons [12]—which probe the local vorticity of the fluid.

Hydrodynamic [5] and transport [13,14] simulations each reproduce rather well the measured "global" polarization, the component directed along the total angular momentum of the collision, $\vec{J}$. In most hydrodynamic calculations, particle properties (e.g., momentum and flavor) are derived from fluid properties (e.g., stress-energy tensor and chemical potentials) through the Cooper-Frye ansatz [5], which assumes equilibrium at the point of hadronization. This formalism has been generalized [15] to calculate particle polarization directly from the thermal vorticity [5] of the fluid. Equilibration of orbital angular momentum and spin degrees of freedom is assumed, though spin relaxation times are not fully understood [16]. In transport simulations, the vorticity is calculated from the particles in small cells, and polarization is extracted through the generalized Cooper-Frye formalism discussed above.

The first measurement of $\overline{P}_H$ by the STAR Collaboration at $\sqrt{s_{NN}} = 62.4$ and 200 GeV was consistent with zero [9]; however, subsequent measurements across a range of lower collision energies $7.7 \leqslant \sqrt{s_{NN}} \leqslant 39$ GeV and with higher statistics at $\sqrt{s_{NN}} = 200$ GeV by the STAR Collaboration showed statistically significant $\overline{P}_H > 0$ [10,17]. Together with high-statistics measurements at $\sqrt{s_{NN}} = 2.76$ and 5.02 TeV by the ALICE Collaboration showing $\overline{P}_H$ consistent with zero, these measurements demonstrated a rising $\overline{P}_H$ with decreasing $\sqrt{s_{NN}}$ [10,11,17].

While a simple extrapolation of this trend would suggest that $\overline{P}_H$ continues to rise as $\sqrt{s_{NN}}$ decreases, we expect vanishing $\overline{P}_H$ at $\sqrt{s_{NN}} = 2m_N$ due to the lack of system angular momentum [18]. A peak $\overline{P}_H$ therefore likely exists in the region $2m_N \approx 1.9 < \sqrt{s_{NN}} < 7.7$ GeV; recent model calculations predict this peak in the vicinity of $\sqrt{s_{NN}} \approx 3$ GeV [18–20]. Furthermore, these calculations, which at $\sqrt{s_{NN}} \gtrsim 7.7$ GeV agree fairly well with each other and with other higher-$\sqrt{s_{NN}}$ calculations [13,14,19,21,22], diverge for $\sqrt{s_{NN}} \lesssim 7.7$ GeV. Measurements of $\overline{P}_H$ at $\sqrt{s_{NN}} < 7.7$ GeV will provide constraints on which sets of assumptions are valid at such small $\sqrt{s_{NN}}$.

As in previous studies, $\overline{P}_H$ represents the spin polarizations of Λ and $\bar{\Lambda}$ hyperons, $\overline{P}_\Lambda$ and $\overline{P}_{\bar{\Lambda}}$; however, $\bar{\Lambda}$-hyperon yields at $\sqrt{s_{NN}} = 3$ GeV are insufficient for a meaningful study of $\overline{P}_{\bar{\Lambda}}$ and we therefore refer directly to $\overline{P}_\Lambda$. We report in this work our observation of nonzero $\overline{P}_\Lambda$, with a statistical significance of nearly 6σ. This observation raises important questions: What is the spin equilibration timescale, and how does it compare to the thermal equilibration timescale? How viscous is the region of nuclei overlap? Our observation of significant, nonzero global $\overline{P}_\Lambda$ at $\sqrt{s_{NN}} = 3$ GeV is the largest $\overline{P}_\Lambda$ yet observed and the lowest energy at which $\overline{P}_\Lambda$ has been measured.

The dataset discussed in this work was collected in 2018 by the STAR experiment [23]. The STAR detector configuration features the cylindrical geometry characteristic of collider experiments. In order to explore various regions of the QCD phase diagram, RHIC has undertaken a multiyear Beam Energy Scan [24] program, extending observations to lower energies. While the maximum energy of a gold beam in the RHIC ring is 100 GeV per nucleon, the facility is remarkably flexible and beams with energy as low as 3.85 GeV per nucleon can be maintained for reasonable times; thus, the lowest energy measured in beam-on-beam collisions is $\sqrt{s_{NN}} = 7.7$ GeV. However, operating the facility and experiment in fixed-target mode, in which the beam collides with a foil target inside the beam pipe positioned 200 cm away from the center of the Time Projection Chamber (TPC), produces collisions at energies as low as $\sqrt{s_{NN}} = 3$ GeV. See Ref. [25] for details of the STAR fixed-target configuration.

Charged-particle tracks in the pseudorapidity range $-2 \lesssim \eta \lesssim 0$ are measured in the TPC [26]. For $-1.5 \lesssim \eta \lesssim 0$, additional identification is performed by time-of-flight measurements in the Barrel Time-of-Flight (BTOF) detector [27,28]. At $\eta < -2.55$, charged particles are registered in the Event Plane Detector (EPD) [29]. Pseudorapidity is reported in the laboratory frame while rapidity, y, is reported in the collision center-of-momentum frame, boosted by the beam rapidity, $y_{\mathrm{beam}} = 1.045$. After basic offline selections to ensure that the reconstructed collision occurred in the target foil, 253×10^6 events were available for this analysis.

The centrality of an event, which describes the degree to which the colliding nuclei overlap, was estimated based on the number of "primary" tracks, which are mainly determined by checking if a track's helical path comes within 3 cm of the primary vertex. Fitting this multiplicity distribution to a Monte Carlo Glauber model [30] calculation provided a measure of the centrality and an estimate of the trigger efficiency. Details of the Glauber calculation for STAR fixed-target measurements are given in Ref. [25].

Protons and pions measured in the TPC were used to reconstruct Λ hyperons, which decay via $\Lambda \to p + \pi^-$ 63.9% of the time [31]. Hyperon candidates were constructed through decay topology with quality assurance selections, such as the distance of closest approach (DCA) between the reconstructed Λ-hyperon trajectory and the primary vertex, and the DCA between the two daughters. Details on the Λ-hyperon reconstruction may be found in Refs. [17,32,33]. Additional important kinematic selection criteria, or "cuts," include $p_T > 0.4$ GeV/c on daughter protons, to avoid contamination with spallation particles, and $p_T > 0.15$ GeV/c on daughter pions, as tracking efficiency in STAR drops quickly for lower values of transverse momentum. Finally, we select Λ hyperons with $p_T > 0.7$ GeV/c as the checks for unknown systematic effects fail below $p_T = 0.7$ GeV/c, and reconstruction efficiency on Λ hyperons also becomes very small below $p_T = 0.7$ GeV/c. Our coverage in rapidity was in the range $-0.2 < y < 1.0$. The typical ratio of true Λ-hyperon yield to combinatoric background near $m_{\mathrm{inv}} = m_{\Lambda,\mathrm{PDG}}$ is 10:1.

The parity-violating nature of hyperon decay reveals the spin polarization, $\vec{P}_\Lambda$. The global polarization is the projection of $\vec{P}_\Lambda$ along the direction of the angular momentum of the collision, $\hat{J}$ [5,9]; in the case of a symmetric collision system and detector setup we may write this as [10]

$$\overline{P}_\Lambda \equiv \langle \vec{P}_\Lambda \cdot \hat{J} \rangle = \frac{8}{\pi \alpha_\Lambda} \frac{1}{R_{\mathrm{EP}}^{(1)}} \langle \sin(\Psi_1 - \phi_p^*) \rangle^{\mathrm{sig}}. \quad (1)$$

Here, $\alpha_\Lambda = 0.732 \pm 0.014$ is the Λ-hyperon decay constant [31], ϕ_p^* is the azimuthal angle of the daughter proton momentum in the Λ-hyperon rest frame, and the average is over all hyperons in the momentum range selected. Ψ_1 is the first-order event plane of the collision, and $R_{\mathrm{EP}}^{(1)}$ is the resolution with which the event plane estimates the reaction plane of the collision, which is normal to $\hat{J}$. The "sig" label indicates that the average excludes combinatoric-background contributions and acceptance effects; we discuss these below. As we will see later, the symmetries required to achieve the form of Eq. (1) are broken when operating RHIC/STAR in fixed-target mode.

Charged particles with $-2.84 < \eta < -2.55$, measured in the outer four rings of the EPD, are used to determine Ψ_1 [29],

and the three-subevent method [34] is used to measure $R_{\mathrm{EP}}^{(1)}$. The two reference subevents used in this method use particles measured at $-0.5 < \eta < -0.4$ and $-0.2 < \eta < -0.1$ in the TPC. In this analysis, the event-plane resolution $R_{\mathrm{EP}}^{(1)} \approx 40\%$ for 20–50 % central collisions. Because the STAR magnetic field along $\hat{z}$ causes charged particles to curve and also because produced particles are disproportionately positive as $\sqrt{s_{\mathrm{NN}}}$ becomes smaller, Ψ_1 as measured by the EPD is twisted by an angle $\Delta\Psi_{1,\mathrm{EPD}}$. $\Delta\Psi_{1,\mathrm{EPD}}$ can be calculated by correlating $\Psi_{1,\mathrm{EPD}}$ with $\Psi_{1,\mathrm{TPC}}$, as the TPC is able to trace tracks to the collision point and therefore does not suffer this rotation effect; $\Delta\Psi_{1,\mathrm{EPD}} = 0.063 \pm 0.011$ by which we correct $\Psi_{1,\mathrm{EPD}}$.

A fraction of $[p, \pi^-]$ pairs that enter our analysis will not arise from true hyperons, but will instead originate from combinatorial background. To statistically extract the true polarization signal from the false background signal, we used the invariant-mass method [17,35,36], in which the observed $\langle \sin(\Psi_1 - \phi_p^*) \rangle$ is measured as a function of invariant mass and written as a sum of signal and background contributions:

$$\langle \sin(\Psi_1 - \phi_p^*) \rangle^{\mathrm{obs}}(m_{\mathrm{inv}})$$
$$= f^{\mathrm{bg}}(m_{\mathrm{inv}}) \langle \sin(\Psi_1 - \phi_p^*) \rangle^{\mathrm{bg}}$$
$$+ (1 - f^{\mathrm{bg}}(m_{\mathrm{inv}})) \langle \sin(\Psi_1 - \phi_p^*) \rangle^{\mathrm{sig}}. \quad (2)$$

Here, $\langle \sin(\Psi_1 - \phi_p^*) \rangle^{\mathrm{sig}}$ is the average Λ-hyperon polarization, while the term $\langle \sin(\Psi_1 - \phi_p^*) \rangle^{\mathrm{bg}}$ is the false polarization of the combinatoric background. The combinatoric fraction $f^{\mathrm{bg}}(m_{\mathrm{inv}})$ is extracted through fits to the m_{inv} distribution.

The direction of the STAR magnetic field, $\vec{B}_{\mathrm{STAR}}$, which is aligned with the direction of the beam momentum $(-\hat{z})$ in the laboratory frame, drives charged particles to follow helical paths and breaks a right-left symmetry in the Λ-hyperon decay. Consider a "right" and a "left" class of decays. A "right" decay is one in which the proton decays to the right side of the Λ hyperon as viewed along $-\hat{z}$, or equivalently when $(\vec{p}_\Lambda \times \vec{p}_p^*) \cdot \vec{B}_{\mathrm{STAR}} > 0$. A "left" decay simply flips the sign of $\vec{p}_p^*$. Due to their helical paths, the tracks of daughters from "left" decays diverge while those from "right" decays cross paths in the transverse plane. STAR's Λ-hyperon reconstruction efficiency, resolution, and purity therefore depend on $(\vec{p}_\Lambda \times \vec{p}_p^*) \cdot \vec{B}_{\mathrm{STAR}}$, leading to the differences in the invariant-mass spectra shown in Fig. 1. Directed flow, v_1, modulates the yield of Λ hyperons as $\sim(1 + v_1 \cos(\phi_\Lambda - \Psi_1))$ [37] and in fixed-target mode our acceptance is greater for $y > 0$ than for $y < 0$; there is therefore a net directed flow when integrating over all Λ hyperons such that ϕ_Λ is positively correlated with Ψ_1.

Recall the polarization correlator, $\langle \sin(\Psi_1 - \phi_p^*) \rangle$, from Eq. (2); because of the net, flow-driven correlation between ϕ_Λ and Ψ_1, the aforementioned "right" ("left") decay will correspond to $\langle \sin(\Psi_1 - \phi_p^*) \rangle > 0 (< 0)$. Since "left" decays also have a wider m_{inv} distribution, they dominate the sides of the net m_{inv} distribution while "right" decays dominate the center. The observed net polarization correlation term from Eq. (2) is therefore sharply peaked and positive for $m_{\mathrm{inv}} \approx m_{\Lambda,\mathrm{PDG}}$, and becomes negative as $|m_{\mathrm{inv}} - m_{\Lambda,\mathrm{PDG}}|$ becomes larger, and therefore does not follow the form of the observed net $f^{\mathrm{sig}}(m_{\mathrm{inv}})$. For this reason, we generalize the invariant-
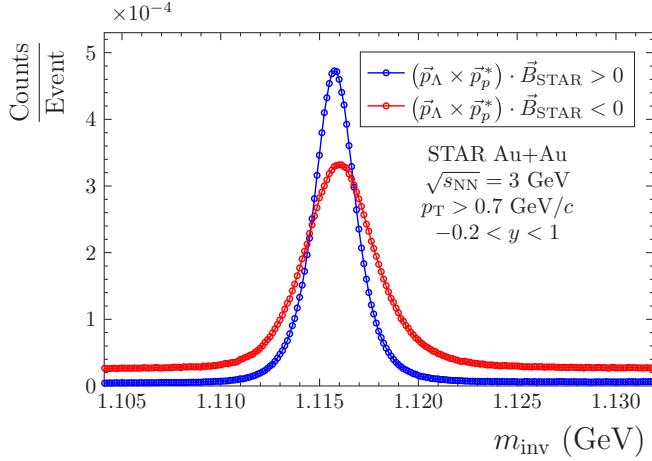
FIG. 1. The measured m_{inv} distributions of two classes of Λ-hyperon decays: "right" decays in blue, with $(\vec{p}_\Lambda \times \vec{p}_p^*) \cdot \vec{B}_{STAR} > 0$, and "left" decays in red, with $(\vec{p}_\Lambda \times \vec{p}_p^*) \cdot \vec{B}_{STAR} < 0$. The "right" decay class has a notably sharper m_{inv} distribution than the "left" decay class, and this is due to the effects of daughter tracks crossing in the STAR TPC with $\vec{B}_{STAR} || -\hat{z}$. The opposite pattern is obtained by flipping the sign of $\vec{B}_{STAR}$ or by reconstructing $\bar{\Lambda}$ hyperons.

FIG. 2. The signal polarizations extracted according to Eq. (2) as a function of $\phi_\Lambda - \phi_p^*$, for positive-rapidity Λ hyperons. The sinusoidal behavior is driven by nonzero net v_1. The vertical shift corresponds to the vorticity-driven polarization according to Eq. (3); in collider mode, where the net v_1 is zero, this dependence on $\phi_\Lambda - \phi_p^*$ does not exist. The functional form of Eq. (3) fits the data well, with $\chi^2/\mathrm{ndf} = 1.49$.

mass method by performing the method separately for narrow bins in $\phi_\Lambda - \phi_p^*$. By expanding the correlator $\langle \sin(\Psi_1 - \phi_p^*) \rangle$ and taking advantage of the fact that $\langle \sin(\Psi_1 - \phi_\Lambda) \rangle = 0$ through symmetry, each bin in $\phi_\Lambda - \phi_p^*$ has a contribution to $\langle \sin(\Psi_1 - \phi_p^*) \rangle$ proportional to $\langle \sin(\phi_\Lambda - \phi_p^*) \rangle$. Across all bins in $\phi_\Lambda - \phi_p^*$ the net, flow-driven correlation between ϕ_Λ and Ψ_1, present in our data, therefore generates a sinusoidal component in Eq. (1) unrelated to global polarization, so that

$$\frac{8}{\pi \alpha_\Lambda} \frac{1}{R_{EP}^{(1)}} \langle \sin(\Psi_1 - \phi_p^*) \rangle^{sig} = \overline{P}_\Lambda + c \sin(\phi_\Lambda - \phi_p^*), \quad (3)$$

where the coefficient c depends on v_1. Figure 2 shows the signal polarizations extracted using Eq. (2) across small bins in $\phi_\Lambda - \phi_p^*$ and fitted according to Eq. (3). The vertical shift corresponds to $\overline{P}_\Lambda$; this procedure removes any contributions from potentially nonzero polarization in the production plane, spanned by $\vec{p}_\Lambda \times \vec{p}_{beam}$, as seen in Refs. [38,39]. This procedure is performed separately for $y_\Lambda > 0$ and $y_\Lambda < 0$, and the weighted average is extracted. We performed detailed simulations of the STAR acceptance and tracking reconstruction to verify the above procedure to extract $\overline{P}_\Lambda$. Previous analyses [9–11,17] have focused on particles measured near mid-rapidity ($|y| < 1$) and at higher collision energies, where directed flow [34] is small; as well, the Λ-hyperon acceptance is symmetric in y in collider mode. The azimuthal dependencies discussed above were therefore not an issue.

Finite detector acceptance and efficiency necessitate two additional corrections on the measured polarization. Equation (1) assumes that the efficiency to measure daughter protons is independent of $\vec{p}_p^*$, the daughter momentum direction in the hyperon rest frame. However, rapidity cuts and inefficiencies introduce a weak dependence on $\vec{p}_p^*$, leading to a correction factor $\frac{4}{\pi} \overline{\sin \theta_p^*}$ [9] which depends on p_T, y, and centrality
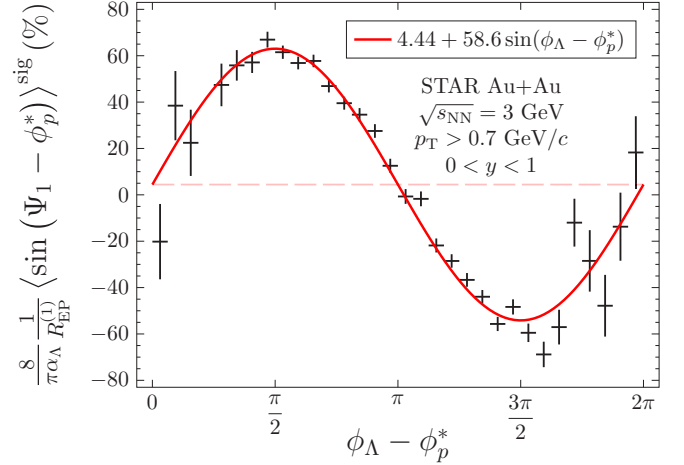
and is $\mathcal{O}(1\%)$. Similarly, the Λ-hyperon detection efficiency, $\varepsilon(y, p_T)$, depends on $\vec{p}_\Lambda$.

A suite of tests was performed to search for unexpected systematic effects [41]. This included analyzing collisions measured at different times during the experiment, checking both time of day and day of the week; restricting the analysis to various regions of ϕ_Λ in the laboratory system; separately analyzing collisions recorded when the collision rate was high or low, or with high or low experimental background rates; changing the Λ-finding algorithm; changing the numerous fit parameters in the invariant-mass method; changing the width in η of the subevent used for Ψ_1 calculation; and changing the set of topological cuts used to identify Λ hyperons. Contributions to systematic uncertainty originate in the uncertainties on our measurements of the corrections. These contributions include a 2% systematic uncertainty associated with the uncertainty [31] on α_Λ; a $<1\%$ statistical uncertainty on $\varepsilon(y, p_T)$ corresponding to the statistical precision of the Monte Carlo simulations; a $<1\%$ statistical uncertainty on $\frac{4}{\pi}\overline{\sin \theta_p^*}$; a $<1\%$ uncertainty on $\Delta\Psi_{1,EPD}$; a $<1\%$ statistical uncertainty on $R_{EP}^{(1)}$; and a $<1\%$ uncertainty arising from the assumptions made about the background polarization's dependence on m_{inv} when applying Eq. (2). These systematic uncertainties are added in quadrature to get the full systematic uncertainty.

Figure 3 shows the global polarization at mid-rapidity, alongside previous measurements whose data points have been scaled according to the updated decay parameter $\alpha_\Lambda = 0.732$ [31]. The polarization of $\overline{P}_\Lambda = 4.91 \pm 0.81(\text{stat.}) \pm 0.15(\text{syst.})\%$, reported in this paper, is the largest global Λ-hyperon polarization yet observed. We find that the steady increase of $\overline{P}_\Lambda$ with decreasing $\sqrt{s_{NN}}$ continues almost to the Λ-hyperon production threshold.

Nevertheless, this trend has been reproduced by hydrodynamic and transport calculations [5,13,14,21] above $\sqrt{s_{NN}} =$
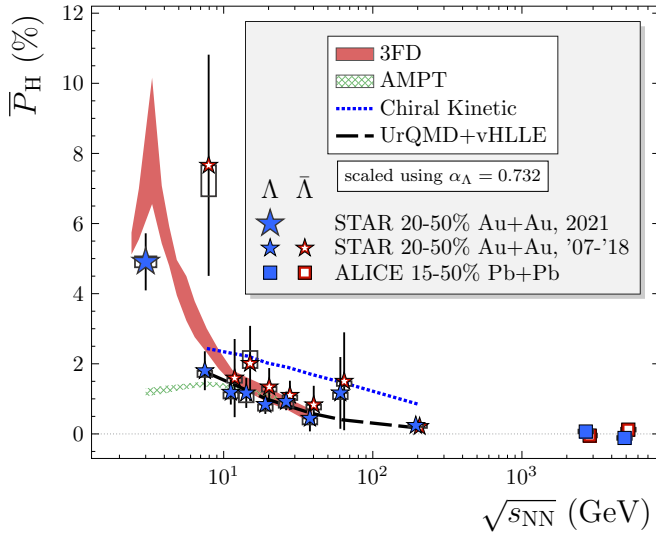
FIG. 3. Global hyperon polarization as a function of $\sqrt{s_{NN}}$ in mid-central heavy-ion collisions. The trend of increasing $\overline{P}_H$ with decreasing $\sqrt{s_{NN}}$ is maintained at the low energy of $\sqrt{s_{NN}} = 3$ GeV. Statistical uncertainties are represented with lines while systematic uncertainties are represented with boxes. Previous experimental results [9–11,17] are scaled [5] using the currently accepted [31] decay parameter $\alpha_\Lambda = 0.732$. Calculations with a hybrid model (UrQMD+vHLLE) [22] and chiral-kinetic transport [21] are compared to the higher-$\sqrt{s_{NN}}$ data only, while others have been extended to lower energy. The AMPT model [20] matches higher-energy data well while dramatically underestimating $\overline{P}_\Lambda$ at $\sqrt{s_{NN}} = 3$ GeV. The hydrodynamic 3FD model [40] with two separate equations of state (crossover and first-order phase transition) predicts a sharply rising $\overline{P}_\Lambda$ below $\sqrt{s_{NN}} = 7.7$ GeV. The models shown use an impact parameter of 8 fm.

7.7 GeV. Vorticity from the three-fluid hydrodynamics (3FD) [40] as well as partonic-transport (AMPT) [20] calculations have been extended to the lowest energies, as shown in Fig. 3. For the hydrodynamic 3FD calculation, $\vec{\omega}_{th}$ is calculated directly from the local flow and temperature distributions. In the AMPT calculations, the thermal vorticity is calculated in coarse-grained "cells" from particle ensembles [14].

Polarizations predicted by 3FD calculations depend on the range of hydrodynamic rapidity $y_h \equiv \ln[(u_0 + u_z)/(u_0 - u_z)]$ of the fluid contributing to the Λ hyperons [42]. The shaded band representing the 3FD model in Fig. 3 corresponds to varying the selection between $|y_h| < 0.35$ and $|y_h| < 0.6$. Calculations were performed using one equation of state in which the deconfinement transition is characterized as first order and using another assuming a crossover transition; the resulting difference in polarization between these two methods is much smaller than the width of the band.

We find that, while the central value of the 3FD calculation [40] overshoots the measurement at $\sqrt{s_{NN}} = 3$ GeV by $\sim 30\%$, the prediction and our measurement roughly agree within uncertainties. The partonic-transport calculation [20], which reproduces the measurements quite well at $\sqrt{s_{NN}} \geqslant 7.7$ GeV, dramatically underestimates $\overline{P}_\Lambda$ at $\sqrt{s_{NN}} = 3$ GeV; the model was tuned for very low collision energy and there-
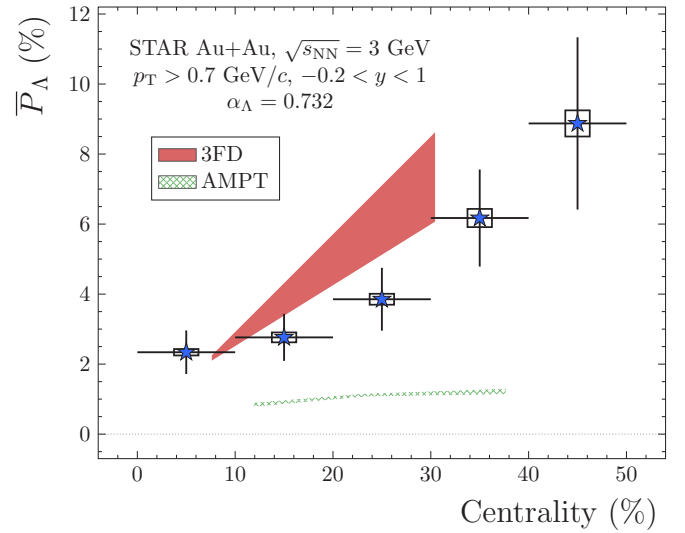

FIG. 4. The centrality dependence of $\overline{P}_\Lambda$ is compared with partonic-transport [20] and three-fluid hydrodynamic [40] calculations at impact parameters of 8 fm. Statistical uncertainties are represented with lines while systematic uncertainties are represented with boxes.

fore differs from previous calculations using the same model at larger $\sqrt{s_{NN}}$ [14,43,44]. The difference between the predictions made using the 3FD and AMPT models becomes larger at low collision energy and suggests that the polarization is strongly dependent on the state of the system. We observe rough agreement with the calculations made using the 3FD model, which may imply that the system evolves hydrodynamically even at low collision energies. At a more general level than $\sim 1\sigma$ discrepancies, the observation of large polarization demonstrates that the hadron gas supports enormous vorticity at low collision energies.

As seen in Fig. 4, we observe larger hyperon polarization for more peripheral collisions, consistent with the increased
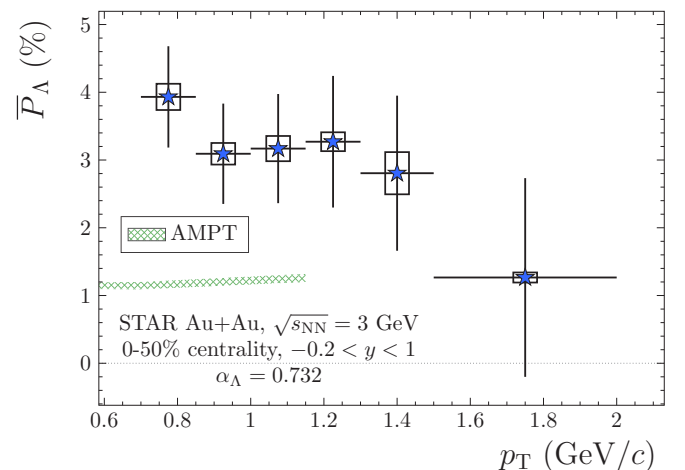

FIG. 5. The p_T dependence of $\overline{P}_\Lambda$ is compared with AMPT [20] at an impact parameter of 8 fm. We observe no dependence within uncertainties. Statistical uncertainties are represented with lines while systematic uncertainties are represented with boxes.
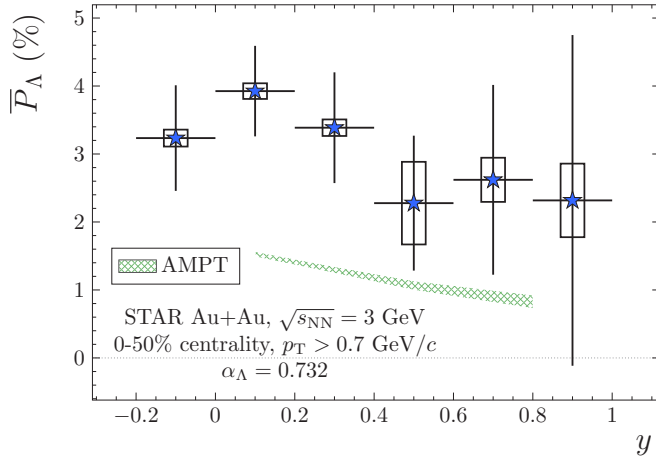
FIG. 6. The y dependence of $\overline{P}_\Lambda$ is compared with AMPT [20] at an impact parameter of 8 fm. We observe no dependence within uncertainties, even for the most forward Λ hyperons. Statistical uncertainties are represented with lines while systematic uncertainties are represented with boxes.

global angular momentum in the system [45]. This expectation is borne out by the 3FD calculations as well as the partonic-transport calculations, though the overall scale of the latter is much lower than the data. A similar dependence of $\overline{P}_H$ was observed in collisions at two orders of magnitude higher energy, $\sqrt{s_{NN}} = 200$ GeV [17]. In Fig. 5, $\overline{P}_\Lambda$ is seen to be independent of transverse momentum, within uncertainties, similar to the lack of dependence seen in top-energy RHIC collisions [17]. At both $\sqrt{s_{NN}} = 3$ and 200 GeV [17], partonic-transport calculations predict only a mild dependence.

Global polarization is directly related to $\vec{J}$, a manifestly three-dimensional phenomenon correlating transverse and longitudinal degrees of freedom. However, $\overline{P}_H$ decreases with increasing collision energy, even as $|\vec{J}|$ increases with $\sqrt{s_{NN}}$; cf. Fig. 3. This may be partly due to longer evolution times at higher energies, increasing the viscosity-driven decay of vorticity before polarized hyperon emission [46]. An increased system temperature at higher $\sqrt{s_{NN}}$ may also play a small role in decreased polarization [47]. Several models associate the $\sqrt{s_{NN}}$ dependence of $\overline{P}_H$ with the vorticity becoming increasingly concentrated at forward rapidity, $|y| \gtrsim 1$–1.5, including transport [45], hydrodynamics [19,42,48,49], and geometric-driven calculations [50]. Correspondingly, these models predict a strong increase of $\overline{P}_H$ as $|y|$ is increased. Still other calculations predict a dramatic reduction of $\overline{P}_H$ away from mid-rapidity [43,51,52]. In most models, the dependence becomes stronger at lower $\sqrt{s_{NN}}$ since higher-energy collisions better approximate boost invariance in the mid-rapidity region.

While all previous measurements were confined to the region $|y| \ll |y_{beam}|$ and were unable to reconstruct forward-rapidity Λ hyperons, the present measurement covers the range $-0.2 \leqslant y \lesssim y_{beam}$ which reaches the upper limit of y_Λ at this collision energy. As shown in Fig. 6, we find no significant dependence of $\overline{P}_\Lambda$ on rapidity, though statistical uncertainties are relatively large and a loose centrality selection is used. This is already sufficiently precise to disagree with the prediction of AMPT.

Our measurement of nonzero $\overline{P}_\Lambda$ at $\sqrt{s_{NN}} = 3$ GeV demonstrates that vorticity aligned with $\hat{J}$ is at a maximum below $\sqrt{s_{NN}} = 7.7$ GeV. The data agree roughly with calculations made using the 3FD model, integrated over mid-rapidity, but are dramatically larger than such calculations made using the partonic-transport model AMPT. As in Ref. [17], we observe a significant centrality dependence of $\overline{P}_\Lambda$ that is consistent with increasing $\vec{J}$. Our measurement of the dependence of $\overline{P}_\Lambda$ on y is uniquely valuable because we have access to the most forward-rapidity Λ hyperons. Interestingly, despite the variety of model calculations predicting quite strong dependence of $\overline{P}_H$ on y [19,42,43,45,48–52], we see no statistically significant dependence. A migration of $\overline{P}_H$ towards forward rapidity has been offered as a potential explanation of the monotonic fall of $\overline{P}_H$ with $\sqrt{s_{NN}}$ [45]. Given our observation, such an explanation may be incorrect, though this does not dispel such arguments as the state of the system at higher energy is notably different; measurements of $\overline{P}_H$ using the STAR forward upgrade will provide indispensable comparisons to the work presented here.

[1] Y. Akiba *et al.*, arXiv:1502.02730.

[2] D. A. Teaney, in *Quark-Gluon Plasma 4*, edited by R. C. Hwa and X.-N. Wang (World Scientific, Singapore, 2010), pp. 207–266.

[3] U. W. Heinz, J. Phys.: Conf. Ser. **455**, 012044 (2013).

[4] J. E. Bernhard, J. S. Moreland, S. A. Bass, J. Liu, and U. Heinz, Phys. Rev. C **94**, 024907 (2016).

[5] F. Becattini and M. A. Lisa, Annu. Rev. Nucl. Part. Sci. **70**, 395 (2020).

[6] Z.-T. Liang and X.-N. Wang, Phys. Rev. Lett. **94**, 102301 (2005); **96**, 039901(E) (2006).

[7] F. Becattini, F. Piccinini, and J. Rizzo, Phys. Rev. C **77**, 024906 (2008).

[8] B. Betz, M. Gyulassy, and G. Torrieri, Phys. Rev. C **76**, 044901 (2007).

[9] B. I. Abelev *et al.* (STAR Collaboration), Phys. Rev. C **76**, 024915 (2007); **95**, 039906 (2017).

[10] L. Adamczyk *et al.* (STAR Collaboration), Nature (London) **548**, 62 (2017).

[11] S. Acharya *et al.* (ALICE Collaboration), Phys. Rev. C **101**, 044611 (2020).

[12] J. Adam *et al.* (STAR Collaboration), Phys. Rev. Lett. **126**, 162301 (2021).

[13] O. Vitiuk, L. V. Bravina, and E. E. Zabrodin, Phys. Lett. B **803**, 135298 (2020).

[14] H. Li, L.-G. Pang, Q. Wang, and X.-L. Xia, Phys. Rev. C **96**, 054908 (2017).

[15] F. Becattini, V. Chandra, L. Del Zanna, and E. Grossi, Ann. Phys. **338**, 32 (2013).

[16] S. Bhadury, W. Florkowski, A. Jaiswal, A. Kumar, and R. Ryblewski, Phys. Lett. B **814**, 136096 (2021).

[17] J. Adam *et al.* (STAR Collaboration), Phys. Rev. C **98**, 014910 (2018).

[18] X.-G. Deng, X.-G. Huang, Y.-G. Ma, and S. Zhang, Phys. Rev. C **101**, 064908 (2020).

[19] Y. B. Ivanov, V. D. Toneev, and A. A. Soldatov, Phys. Rev. C **100**, 014908 (2019).

[20] Y. Guo, J. Liao, E. Wang, H. Xing, and H. Zhang, Phys. Rev. C **104**, L041902 (2021).

[21] Y. Sun and C. M. Ko, Phys. Rev. C **96**, 024906 (2017).

[22] I. Karpenko and F. Becattini, Eur. Phys. J. C **77**, 213 (2017).

[23] K. H. Ackermann *et al.* (STAR Collaboration), Nucl. Instrum. Methods A **499**, 624 (2003).

[24] M. M. Aggarwal *et al.* (STAR Collaboration), arXiv:1007.2613.

[25] J. Adam *et al.* (STAR Collaboration), Phys. Rev. C **103**, 034908 (2021).

[26] M. Anderson *et al.*, Nucl. Instrum. Methods A **499**, 659 (2003).

[27] W. J. Llope (STAR Collaboration), Nucl. Instrum. Methods A **661**, S110 (2012).

[28] M. Shao, O. Y. Barannikova, X. Dong, Y. Fisyak, L. Ruan, P. Sorensen, and Z. Xu, Nucl. Instrum. Methods A **558**, 419 (2006).

[29] J. Adams *et al.*, Nucl. Instrum. Methods A **968**, 163970 (2020).

[30] R. L. Ray and M. Daugherity, J. Phys. G **35**, 125106 (2008).

[31] P. A. Zyla *et al.* (Particle Data Group), Prog. Theor. Exp. Phys. **2020**, 083C01 (2020).

[32] S. Gorbunov, Ph.D. thesis, Johann Wolfgang Goethe University (2013).

[33] M. Zyzak, Ph.D. thesis, Johann Wolfgang Goethe University (2015).

[34] A. M. Poskanzer and S. A. Voloshin, Phys. Rev. C **58**, 1671 (1998).

[35] L. Adamczyk *et al.* (STAR Collaboration), Phys. Rev. C **88**, 014902 (2013).

[36] N. Borghini and J. Y. Ollitrault, Phys. Rev. C **70**, 064905 (2004).

[37] S. A. Voloshin, A. M. Poskanzer, and R. Snellings, in *Collective Phenomena in Non-Central Nuclear Collisions*, edited by R. Stock (Springer-Verlag, Berlin Heidelberg, 2010).

[38] A. Lesnik, D. M. Schwartz, I. Ambats, E. Hayes, W. T. Meyer, C. E. W. Ward, T. M. Knasel, E. G. Swallow, R. Winston, and T. A. Romanowski, Phys. Rev. Lett. **35**, 770 (1975).

[39] G. Bunce *et al.*, Phys. Rev. Lett. **36**, 1113 (1976).

[40] Y. B. Ivanov, Phys. Rev. C **103**, L031903 (2021).

[41] R. Barlow, in *Conference on Advanced Statistical Techniques in Particle Physics* (Durham University, Durham, UK, 2002), pp. 134–144.

[42] Y. B. Ivanov and A. A. Soldatov, Phys. Rev. C **102**, 024916 (2020).

[43] D.-X. Wei, W.-T. Deng, and X.-G. Huang, Phys. Rev. C **99**, 014905 (2019).

[44] S. Shi, K. Li, and J. Liao, Phys. Lett. B **788**, 409 (2019).

[45] Y. Jiang, Z.-W. Lin, and J. Liao, Phys. Rev. C **94**, 044910 (2016); **95**, 049904(E) (2017).

[46] I. Karpenko and F. Becattini, Nucl. Phys. A **967**, 764 (2017).

[47] D. J. Wang, Z. Néda, and L. P. Csernai, Phys. Rev. C **87**, 024908 (2013).

[48] Y. B. Ivanov and A. A. Soldatov, Phys. Rev. C **97**, 044915 (2018).

[49] H.-Z. Wu, L.-G. Pang, X.-G. Huang, and Q. Wang, Phys. Rev. Res. **1**, 033058 (2019).

[50] Z.-T. Liang, J. Song, I. Upsal, Q. Wang, and Z.-B. Xu, Chin. Phys. C **45**, 014102 (2021).

[51] W.-T. Deng and X.-G. Huang, Phys. Rev. C **93**, 064907 (2016).

[52] Y. Xie, D. Wang, and L. P. Csernai, Eur. Phys. J. C **80**, 39 (2020).